

Multi-stage phase transformation pathways in MAX phases

Received: 29 April 2024

Accepted: 31 January 2025

Published online: 12 February 2025



Shuang Zhao¹, Hao Xiao¹, Yuxin Li¹, Zijun Zhang¹, Yugang Wang¹,
Qing Huang², Liuxuan Cao³, Fei Gao⁴, Cameron L. Tracy⁵,
Rodney. C. Ewing^{5,6} & Chenxu Wang¹✉

Diverse, multi-stage phase transformations occur in many materials under extreme environments. In response to irradiation, some MAX phase compositions transform from an initial hexagonal structure to an intermediate γ -phase, then to a face-centered cubic (fcc) structure, while others instead become amorphous. To date, no comprehensive description of the associated transformation mechanisms, or of the influence of composition on this phase behavior, has been reported. In this work, we combine in situ ion irradiation, Transmission electron microscopy (TEM), and density-functional theory (DFT) calculations to demonstrate the distinct transformation pathways and corresponding energetics of the γ -to-fcc transformation in a series of MAX phases. We show that structural distortion and bond covalency of the intermediate γ -phase determine the outcome of the transformation process. This yields a generalized rule to predict the phase transition behaviors of MAX phases based on their atomic radii and electronegativity. These results provide an insight into the multi-stage phase transformation pathways along which MAX phase systems and related complex materials evolve in extreme environments.

Understanding and predicting phase transformations is one of the crucial tasks of condensed matter physics and materials science. Irradiation, which induces lattice atom displacement, is a common means of probing phase transformation dynamics, since irradiation can provide the driving force for overcoming the energy barrier between stable and metastable phases¹. Study of irradiation-induced polymorphism has been used to elucidate transformation mechanisms in a broad range of both ionic-covalent^{2–6} and metallic materials^{7,8}. Many materials undergo multi-stage phase transformations under irradiation, such as the transition of pyrochlore- or spinel-structured complex oxides first to disordered defect-fluorite structures, then to amorphous structures as irradiation proceeds^{3,4,9}.

MAX phases show similar behavior in response to irradiation. These ternary layered carbides/nitrides, known as metallic ceramics^{10–12}, have been proposed as candidate materials for wide-

ranging applications due to their unique properties, such as nuclear fuel cladding materials and joint materials^{13–16}. They also exhibit a unique multiphase transformation from an initial hex-phase (hexagonal structure) to a γ -phase (hexagonal close-packed structure), and then to a fcc-phase (face-centered cubic structure) under irradiation^{17–21}. However, almost all analyses to date were based on the initial phase or structure, and the role of intermediate phases in the transformation process has been rarely studied. It is a challenge to understand the mechanisms by only analyzing the initial phases. For example, antisite defect formation energy in the initial phases was considered as a criterion to assess the resistance to the irradiation-induced phase transformation, yet this approach cannot fully explain the phase behavior or offer a generalizable predictive capability, since it is restricted to the early stages of the phase transformation process, prior to the formation of the intermediate γ -phase^{17,22}.

¹State Key Laboratory of Nuclear Physics and Technology, Center for Applied Physics and Technology, Peking University, Beijing, China. ²Ningbo Institute of Material Technology and Engineering, Chinese Academy of Sciences (CAS), Ningbo, China. ³College of Energy, Xiamen University, Xiamen, China.

⁴Department of Nuclear Engineering and Radiological Science, University of Michigan, Ann Arbor, MI, USA. ⁵Center for International Security and Cooperation (CISAC), Stanford University, Stanford, CA, USA. ⁶Earth and Planetary Sciences, Stanford University, Stanford, CA, USA. ✉e-mail: cxwang@pku.edu.cn

For the material family of MAX phases (over 340 types), previous irradiation experiments were mostly performed under ex situ irradiation conditions, which does not provide direct observation of the evolving atomic structure as a function of irradiation damage level, and thus fails to describe the complete, multi-stage phase transformation pathway. In addition, prior analyses also mainly focused on the initial hexagonal phases^{23–26} and provided only a phenomenological description of irradiation-induced phase behaviors^{18,19,27,28}. No substantial theoretical investigation of compositional trends in the dynamics of these multi-stage phase transformations has been reported, thus far. Hence, there is a clear need for a comprehensive understanding of the multi-stage phase transformation behavior in this class of materials.

In this work, we report an investigation of the distinct phase transformation behaviors of three representative MAX phases, M_2AlC ($M=Cr, V, Nb$), under in situ ion irradiation with real-time TEM observation. The anomalous case of Cr_2AlC is observed, which does not follow the common hex- γ -fcc phase transition pathway as in V_2AlC and Nb_2AlC . Instead, Cr_2AlC follows a hex- γ -amorphous transition pathway, without forming the fcc-phase. Using ab initio calculations, we explain the compositional origin of these phase transformation dynamics. Unlike prior computational work which considered only the energetics of structural transitions from the initial hex-phase^{23–26}, this improved description of phase energetics captures the key role of the intermediate γ -phase in mediating the radiation response. An atomic-scale mechanism for the observed phase behavior is developed through the quantitative description of energetics along the transformation pathway and the underlying characteristics associated with the lattice and electronic structures of the intermediate γ -phase. We ultimately develop a generalized rule for prediction of the extreme environment phase transition behaviors of MAX phases of varying composition based on atomic radius and electronegativity. This method can be potentially extended to similar complex ceramics that undergo multi-stage phase transformations.

Results and discussion

Diverse compositional trends of multi-stage phase transformation pathways

M_2AlC ($M=Cr, V, Nb$) were studied by in situ ion irradiation at the Xiamen Multiple Ion Beam In-situ TEM Analysis Facility²⁹, and compositional trends in their irradiation-induced polymorphism were characterized. The irradiation was conducted using an ion beam of 800 keV Kr^{2+} at room temperature, while an in situ TEM was used to observe and record the phase states and transformation processes during irradiation. Figure 1 shows the in situ selected area electron diffraction (SAED) micrographs along the $[11\bar{2}0]$ direction of Cr_2AlC , V_2AlC , and Nb_2AlC , respectively. For each material, seven SAED patterns were selected, each corresponding to different ion fluences during the irradiation process, represented by the damage level in displacements per atom (dpa). In all three materials, irradiation triggers the formation of intermediate γ -phases with hexagonal close-packed (hcp) structure at relatively low damage level, due to the accumulation of M-Al ($M=Cr, V, Nb$) antisite defects¹⁷, as shown in Fig. 1c, j, q. Both V_2AlC and Nb_2AlC undergo the hex- γ -fcc phase transformation, while this process was not observed in Cr_2AlC . Instead, the intermediate γ - Cr_2AlC phase amorphized starting from ~1.8 dpa, as indicated by the diffuse scattering ring in Fig. 1e–g. These compositional trends indicate that the transformation to the fcc-phase proceeds not from the initial hex-phase, but instead from the intermediate γ -phase. Additionally, the γ -to-fcc phase transformation occurs at a lower irradiation fluence in Nb_2AlC than that in V_2AlC . Further experimental results in Cr_2AlC under Al^+ ion (as self-ion) irradiation confirmed this phase transformation and amorphization process, as shown in Supplementary Fig. S2 in the Supplementary Information. Additionally, prior work also indicates that the same transformation pathway is followed at other irradiation conditions (ions and temperatures), although the transformation rate may differ^{18,27,30}.

Evidence from high-resolution TEM (HRTEM) micrographs

High-resolution TEM (HRTEM) micrographs of Cr_2AlC , V_2AlC (as shown in Fig. 2), and Nb_2AlC (see Supplementary Fig. S3 in the

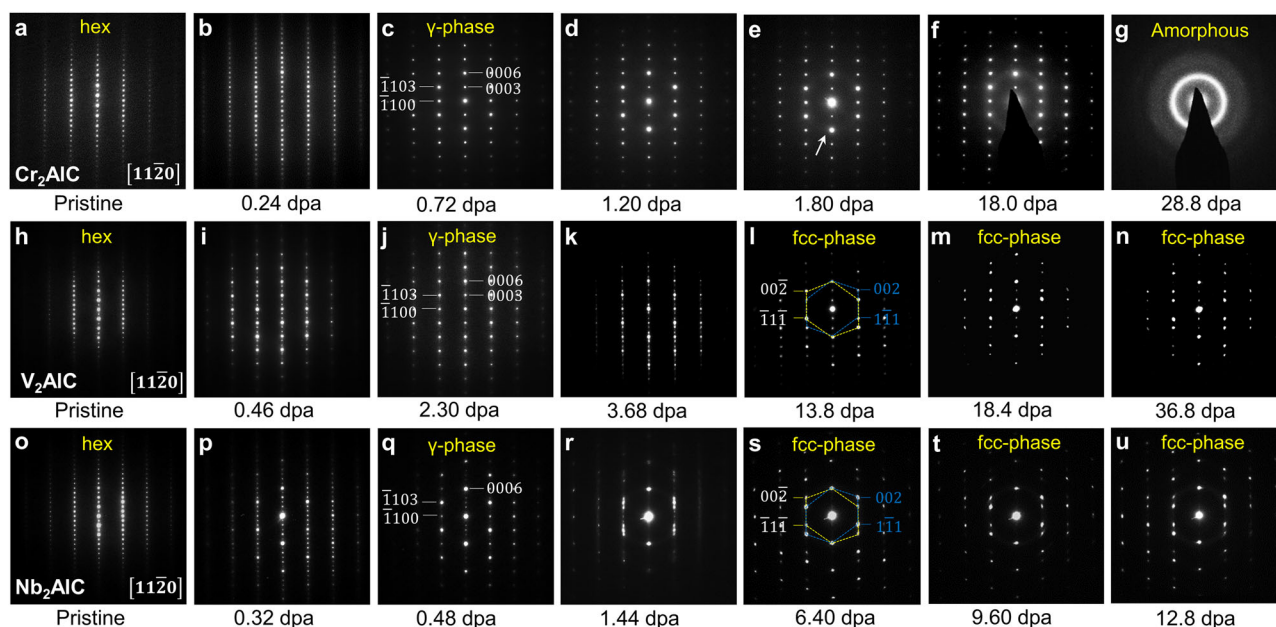
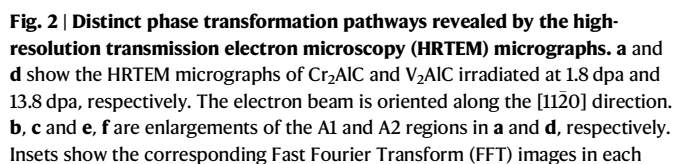


Fig. 1 | Diverse compositional trends of multi-stage phase transformation pathways among M_2AlC ($M=Cr, V, Nb$) under in situ irradiation. The image sequences of (a–g), (h–n) and (o–u) show the selective area electron diffraction (SAED) patterns of Cr_2AlC , V_2AlC and Nb_2AlC along the $[11\bar{2}0]$ direction recorded during 800 keV Kr^{2+} in situ irradiation at room temperature. V_2AlC and Nb_2AlC

transformed to the γ -phase at about 2.3 and 0.48 dpa, respectively, then to the fcc-phase at about 13.8 and 6.4 dpa, respectively. For Cr_2AlC , an amorphous ring appeared at about 1.80 dpa, as marked by the white arrow in e, indicating the transition from the γ -phase to an amorphous state.



As discussed above, this γ -fcc phase transformation process is strongly related to the accumulation of SFs bounded by dislocation gliding. Thus, to further quantify this process, we calculated the energy pathway for the glide of $\frac{1}{3}\langle 10\bar{1}0 \rangle$ -type Shockley partials through the synchroshear mechanism on successive (0001) planes of the γ -phase in these materials (See Supplementary Fig. S5 in the Supplementary Information). The generalized stacking fault energy (GSFE) profiles (including the stacking-fault energy (SFE) γ_{isf} , and the unstable SFE γ_{us} , which represents the barrier energy E_a to forming an SF⁴³) demonstrate that γ -Cr₂AlC possesses a positive γ_{isf} and has a much higher energy barrier ($E_a^{isf} \sim 901.9 \text{ mJ} \cdot \text{m}^{-2}$) as compared with those of γ -

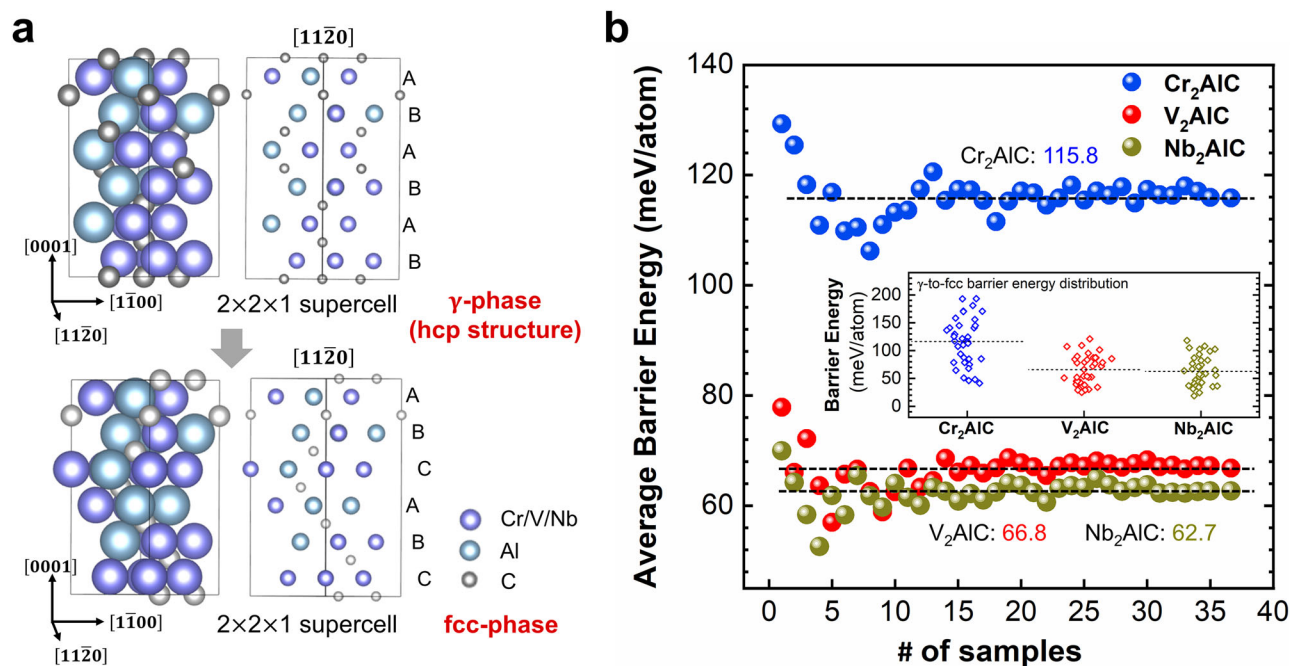


Fig. 3 | Calculated barrier energy along the minimum energy path (MEP) for the γ-to-fcc phase transformation in Cr₂AlC, V₂AlC, and Nb₂AlC. a The side views along [1120] of a special quasirandom structure (SQS) supercell with hcp and fcc structures. **b** The average barrier energy of the γ-to-fcc phase transition with the

number of samples in M₂AlC (M = Cr, V, Nb). The inset shows the corresponding distribution. It is shown that γ-Cr₂AlC has a much higher energy barrier as compared with those of γ-V₂AlC and γ-Nb₂AlC.

V₂AlC and γ-Nb₂AlC (545.5 and 515.5 *mf* · *m*⁻², respectively). These results are consistent with the trend of calculated barrier energies for the γ-to-fcc phase transformation in Fig. 3b.

Correlation of the energetic features with the properties of the γ-phases

Both the experimental and computational results above indicate two distinct phase transformation pathways from the intermediate γ-phase to either fcc or amorphous end states. Therefore, it is essential to focus on the role of the γ-phase in these transformation pathways. We found the energetic features of these phase transformations can be rationalized by the underlying properties of the lattice and the electronic structures of the intermediate γ-phases. To calculate the lattice distortion and bonding characteristic in the γ-M₂AlC (M = Cr, V, Nb) phases, DFT relaxation together with a charge density topology analysis was applied to these crystalline structures (Fig. 4a). The latter was implemented by the Critic2 code⁴⁴ based on the quantum theory of atoms in molecules (QTAIM)⁴⁵, to obtain the charge densities at the bond critical points (BCPs) and then evaluate the covalency of bonds (see further details of this approach in the Supplementary Information). Figure 4b shows the statistical results of the lattice distortion, Δ*d*, and average charge density at the BCPs of M/A-C bonds $\rho(r_b)$ over five 3 × 3 × 1 SQS supercells of γ-M₂AlC (M = Cr, V, Nb) phases and corresponding transformed fcc-phases. The lattice distortion Δ*d*, is described by the atomic deviation from the regular ideal lattice sites as⁴⁶

$$\Delta d = \frac{1}{N} \sum_{i=1}^N \left[(x_i - x'_i)^2 + (y_i - y'_i)^2 + (z_i - z'_i)^2 \right]^{\frac{1}{2}} \quad (2)$$

where (*x_i*, *y_i*, *z_i*) and (*x'_i*, *y'_i*, *z'_i*) are the coordinates of the unrelaxed and relaxed positions of atom *i*, respectively. The ab initio results show that the lattice distortions in Cr₂AlC are larger than those in Nb₂AlC and V₂AlC in both the γ-phase and fcc-phase, which is consistent with the trend of the energy barriers for the γ-to-fcc phase transformation and SF formation (left panel in Fig. 4c). This is because the increase of

lattice distortion generally hinders dislocation movement, obstructing slip on the faulting planes⁴⁷.

A related compositional trend is observed in charge density at the BCPs of M/A-C bonds, $\rho(r_b)$ (where $\rho(r_b)$ in Cr₂AlC is the largest), indicating stronger interatomic bonding^{26,45} in the γ-phase of Cr₂AlC. As proposed by Ogata et al.⁴³, crystalline systems that possess stronger covalent or directional bonding characteristics are expected to be more frustrated and less accommodating to shear strain, as reflected by their higher GSFE. The stacking-fault barrier energy (E_a^{sf}) also illustrates a good correlation to the average $\rho(r_b)$ in γ-M₂AlC (M = Cr, V, Nb), as shown in the right panel of Fig. 4c.

Moreover, the charge density redistribution around the faulting planes has been shown to be an important factor determining SFEs^{43,48}, and a positive correlation between the charge density redistribution (Δ*ρ*) and SFE was reported in metals and related systems^{34,43,49}. Figure 4d shows the differential charge density (Δ*ρ*) contour between the transition state (TS) when forming an SF and the initial state (IS), on the defined charge density fault plane (CDFP, the middle plane between the shifted and unshifted layers, where most of the charge density critical points appear⁴⁹) in γ-M₂AlC (M = Cr, V, Nb) phases. The blue and red regions indicate the gain and loss of electrons during the process, respectively. At any given point on the CDFP, the average absolute value of maximum charge gain or loss (MAX|Δ*ρ*|) over 22 SQS configurations in γ-Cr₂AlC, γ-V₂AlC, and γ-Nb₂AlC are approximately 0.20, 0.12, and 0.11 *e/Bohr*³, respectively. A larger value of MAX|Δ*ρ*| indicates that more electrons are redistributed during the process of SF formation, which incurs a larger energy penalty. These results are consistent with the trend of the GSFE, including the energy barrier (Fig. 3b), for the three materials.

A generalized rule to predict the phase transformation behaviors

To develop generalizable rules that can predict phase behavior in this class of materials, we systematically calculated the SFE and corresponding energy barriers of SF formation in several additional MAX

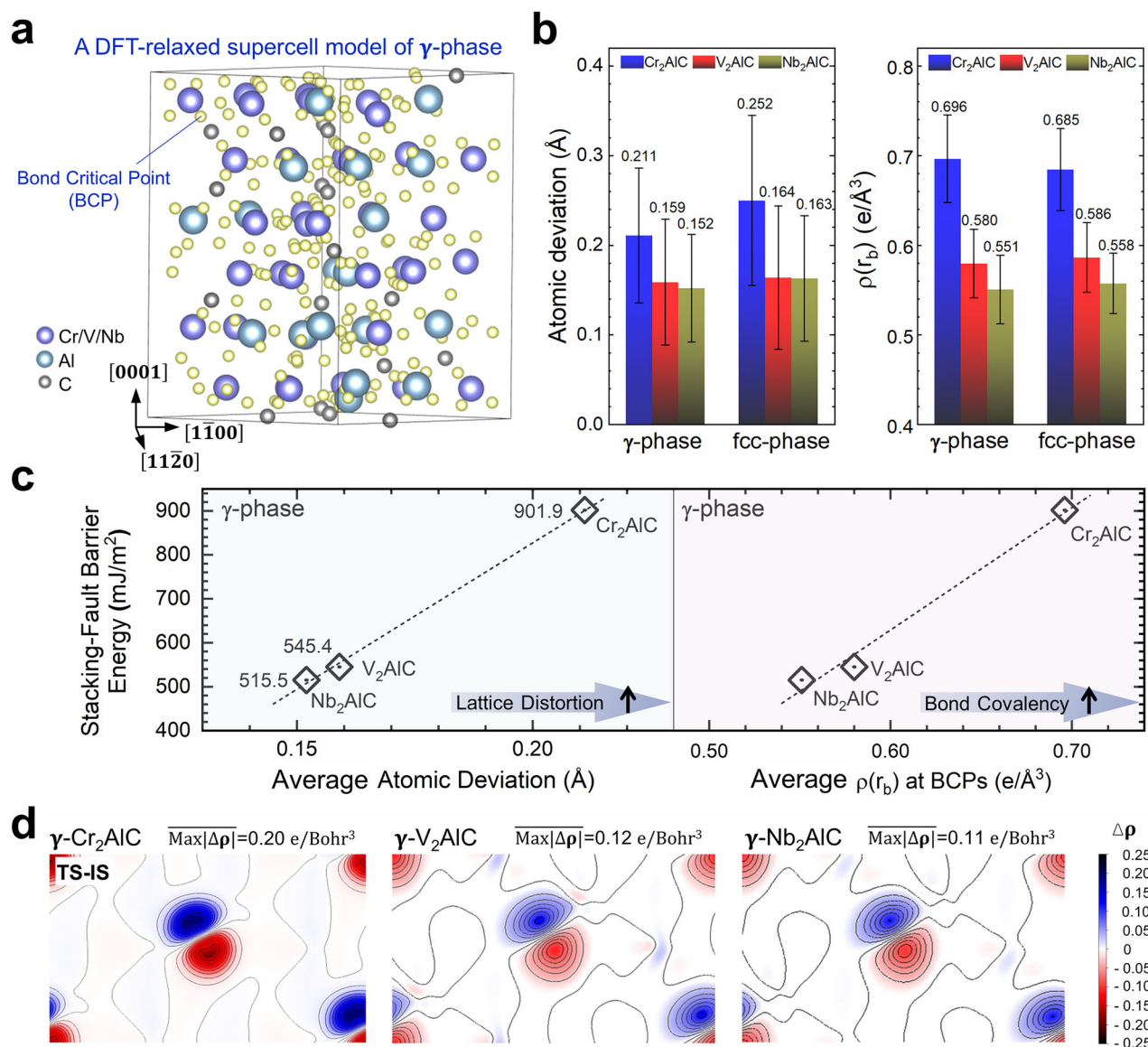


Fig. 4 | Correlation of the generalized stacking fault energy (GSFE) trends with the underlying properties of the lattice and the electronic structures of the intermediate γ -phases. **a** The schematic of a DFT-relaxed $3 \times 3 \times 1$ supercell model of γ - M_2AlC ($\text{M} = \text{Cr}, \text{V}, \text{Nb}$). The yellow spheres represent the bond critical points (BCPs) implemented via the Critic2 code. **b** The DFT calculated lattice distortion (left panel) and average charge density at the BCPs of M/A-C bonds $\rho(r_b)$ (right panel) of the γ -phase and corresponding transformed fcc-phase in M_2AlC ($\text{M} = \text{Cr},$

V, Nb), respectively. The error bar represents the standard deviation (SD).

c Correlations of stacking-fault energy to average atomic deviation (left panel) and average $\rho(r_b)$ (right panel) in γ - M_2AlC ($\text{M} = \text{Cr}, \text{V}, \text{Nb}$), respectively.

d The differential charge density contour plots ($\Delta\rho$) on the defined charge density fault plane (CDFP, which is the middle plane between the shifted and unshifted layers) between the transition state (TS) and the initial state (IS) in one configuration of γ - M_2AlC ($\text{M} = \text{Cr}, \text{V}, \text{Nb}$), due to SF formation.

phases (with γ -phase structures) and investigated the core physical parameters that could estimate and predict the magnitude of the GSFE, which relates to the propensity of a material to transform to the fcc-phase. Two physical parameters, the atomic radius difference between M-A elements (Δr_{M-A}), and the weighted average electronegativity difference between M/A and X elements ($\Delta\chi_{M/A-X}$), correlate well with the stacking-fault barrier energy ($\bar{\gamma}_{us}$ or \bar{E}_a^{isf}), as illustrated in Fig. 5. The atomic radii and electronegativity data are derived from VFI (Vainshtein, Fridkin, Indenbom) atomic radii⁵⁰ and on the Pauling scale⁵¹, respectively. These two fundamental physical parameters are rational indicators to characterize the level of lattice distortion and bond-covalency, respectively, both of which were shown above to play key roles in governing the GSFE, and thus the phase behavior in extreme environments. Generally, the lattice distortion (Δd) increases roughly with the atomic radius difference Δr_{M-A} , as reported in previous studies of both alloys⁴⁶ and

ceramics^{52–54}. As for bonding properties, the M/A-X bond-covalency increases as the $\Delta\chi_{M/A-X}$ decreases^{55,56}. Larger Δr_{M-A} and smaller $\Delta\chi_{M/A-X}$ lead to a higher level of γ_{us} in these MAX phases. These data agree well with the available irradiation experimental results^{18,19,57,58}. For example, Ti_2SnC and Zr_2AlC , with relatively high SF barrier energy, were also observed to become amorphous without undergoing the γ -to-fcc phase transformation under ion irradiation^{57,58}.

Therefore, these general criteria provide a capability for predicting the tendency of stacking fault formation and the phase behavior of these materials under irradiation. These findings further contribute to the understanding of transformation processes and mechanisms in complex materials by revealing the effects of the lattice and electronic structures of intermediate phases on the multi-stage transformation as a whole.

To summarize, we have demonstrated distinct phase transformation pathways in MAX phases (i.e., from a γ -phase, V_2AlC and Nb_2AlC

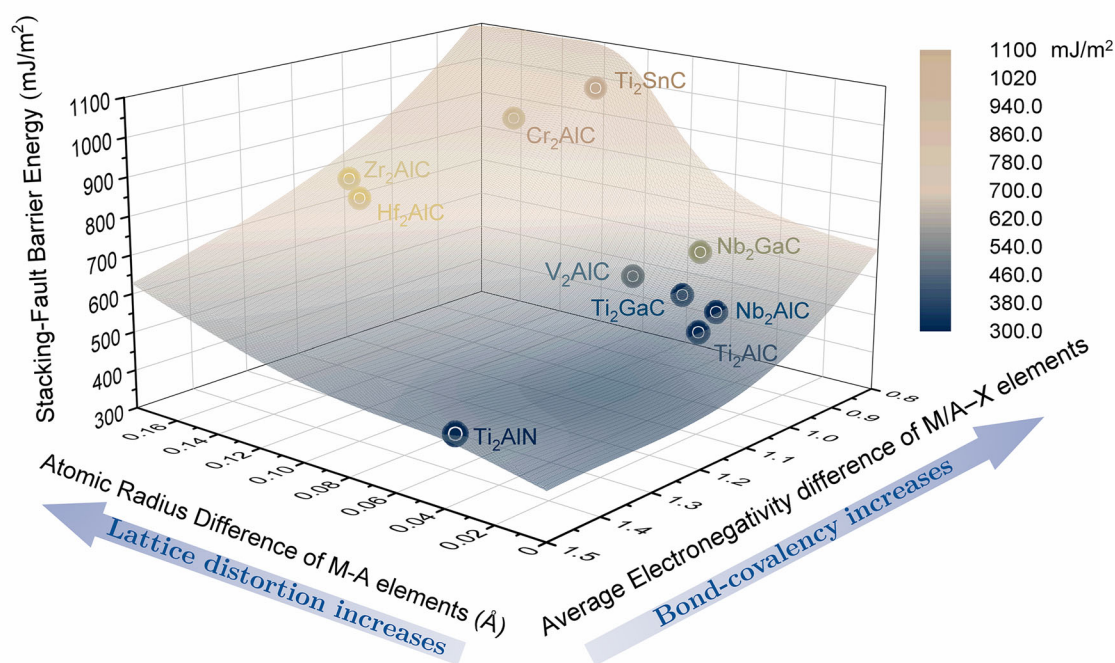


Fig. 5 | Correlation of stacking-fault barrier energy with atomic radii and electronegativity. The stacking-fault barrier energy (E_a^{sf}) of several MAX phases (with γ -phase structures) is revealed to be dependent on the atomic radius difference between M-A elements (Δr_{M-A}), and the weighted average electronegativity

difference between M/A and X elements ($\Delta \chi_{M/A-X}$). Larger Δr_{M-A} and smaller $\Delta \chi_{M/A-X}$ lead to a higher level of stacking-fault barrier energy (γ_{us}) in these γ -phases, and therefore an increased likelihood of amorphization under irradiation.

transform to an fcc-phase while Cr_2AlC instead amorphizes) through in situ ion irradiation with TEM analysis. Using DFT calculations, these compositional effects on the phase transformation behavior under irradiation were interpreted through the quantitative description of GSFE profiles along the transformation pathway from the intermediate γ -phase to the fcc-phase. The larger lattice distortion and stronger bonding covalency in $\gamma\text{-Cr}_2\text{AlC}$ result in a considerably higher transformation energy barrier and GSFE, thus inhibiting the γ -to-fcc phase transformation and instead facilitating amorphization. Based on these findings, a generalized rule to predict the tendency of stacking fault formation and transformation to the fcc-phase in MAX phases was developed based on the atomic radius and electronegativity difference of the constituent elements. By elucidating the atomic-scale processes surrounding the intermediate phases that govern the overall irradiation-induced multi-phase transformation behaviors, these results provide an insight into the relation between composition and phase behaviors in the MAX phase system and related complex materials that undergo multi-stage phase transformations.

Methods

Materials preparation

The Al-based MAX phases irradiated in this work (Cr_2AlC , V_2AlC , Nb_2AlC) were synthesized by an in-situ hot pressing/solid-liquid reaction process at Ningbo Institute of Materials Technology and Engineering (NIMTE), Ningbo, China. The corresponding elemental powders of each material were mixed in stoichiometric proportions, pressed in a graphite die, and subsequently hot-pressed in a flowing Ar atmosphere. More details about the synthesis process have been published elsewhere^{59–61}. The synthesized bulk materials were cut into square specimens and then mechanically thinned to $\sim 20\ \mu\text{m}$ with subsequent polishing. The foils were inserted into $\phi 3$ copper grids, followed by an argon ion milling process from 5 keV down to about 2 keV using a Gatan PIPS 691 ion miller, thus preparing the sample with a thin wedge for in-situ irradiation and transmission electron microscope (TEM) characterization.

Ion irradiation

In-situ ion irradiation experiments for Cr_2AlC , V_2AlC , and Nb_2AlC were conducted using a 400 kV ion implanter coupled with a 300 keV FEI Tecnai F30 transmission electron microscope at Xiamen Multiple Ion Beam In-situ TEM Analysis Facility, Xiamen University²⁹. The ion bombardment was performed with an 800 keV Kr^{2+} beam (twice the accelerating voltage due to the +2 charge) at room temperature (RT). Kr^{2+} ions were chosen since their beam current is relatively stable during irradiation, and their energy transfer efficiency to the target atoms is moderate such that the irradiation-induced phase transformation process can be observed and recorded reasonably. During the in-situ ion irradiation experiments, we monitored the wave shape of the Beam Position Monitor (BPM) and several parameters of the Faraday cylinder, and made timely minor adjustments when the readings deviated, to ensure that the beam current remained at the initial set value. The beam current was set at $-100\ \text{nA}$ ($\sim 2.15 \times 10^{12}\ \text{cm}^{-2}\ \text{s}^{-1}$) in the irradiation experiments, therefore, it took about 2.9 h to get 40 dpa in V_2AlC . During irradiation, selected area electron diffraction (SAED) images were recorded to observe the near real-time phase states and transformations. The radiation damage level (dpa) and the penetration of Kr ions along the ions' incident direction were calculated using the SRIM-2008 program (as shown in Supplementary Fig. S1 in the Supplementary Information). The quick Kinchin-Pease mode was adopted⁶², and the threshold displacement energies for each element were set as 25–28 eV. The Kr^{2+} peak range exceeds the thickness of the TEM sample foil such that the effects of Kr ion accumulation were avoided.

Characterization techniques

TEM observations were obtained using a 200 kV Tecnai F20 transmission electron microscope (FEI, Hillsboro, OR) with a point resolution of 0.24 nm and a line resolution of 0.102 nm at the Electron Microscopy Laboratory of Peking University. In the HRTEM post-processing, we applied a typical HRTEM filter (v1.3, including Wiener and Average Background Subtraction Filter)^{63,64} to avoid potential artifacts. All SAED patterns in each sample were obtained from the same central

part of one grain to avoid the effect of grain boundaries (GBs). To confirm all results, the irradiation experiment was redone in other samples and different grains, and the SAED patterns were checked for consistency.

Computational details

First-principles calculations based on density functional theory (DFT) were conducted in this work applying the Vienna Ab-initio Simulation Package (VASP)⁶⁵. The projector augmented-wave (PAW) method⁶⁶ and the generalized gradient approximation (GGA) by Perdew, Burke, and Ernzerhof (PBE)⁶⁷ were employed for the electron-ion interactions and exchange-correlation function, respectively.

The disordered supercells were constructed using the alloy theoretic automated toolkit (ATAT)⁴⁰ based on the special quasi-random structure (SQS) method⁴¹. The gamma-centered Monkhorst-Pack⁶⁸ k-point of $4 \times 4 \times 2$ is used to sample the Brillouin zone. The total energy and forces converged to better than 10^{-6} eV and 0.01 eV/Å with a plane wave cutoff of 450 eV.

The stacking-fault energy (SFE) γ_{isf} and the unstable SFE γ_{us} (which is the first maximum energy in the GSFE profile) were calculated through the formulas:

$$\gamma_{isf} = \frac{1}{A} (E_{isf} - E_0); \gamma_{us} = \frac{1}{A} (E_{TS} - E_0) \quad (3)$$

where A is the section area of ISF on the (0001) planes, E_0 and E_{isf} represent the energies of the configurations before and after the ISF formed, and E_{TS} is the energy of the corresponding transition state. γ_{us} represents the energy barrier E_a to forming an SF⁴³. This SFE calculation method has also widely used in other material systems^{35,69,70}. The climbing image nudged elastic band (CINEB)⁴² approach was applied to search the transition state and calculate the barrier energy in each step of SF generation, with the number of images inserted being 1 and the spring constant between the images being -5 eV/Å². By comparing the stack fault barrier energies of γ -Cr₂AlC with and without spin polarization, it is found that although considering spin polarization leads to larger fluctuations in the stack fault barrier energies, the average stack fault barrier energies are not significantly different, as shown in Supplementary Fig. S6b in the Supplementary Information. This result suggests that spin polarization does not significantly affect the stack fault barrier energies. Therefore, the calculations were performed without spin polarization. The differential charge density distribution mapping was performed from the three-dimensional visualization program of VESTA for atomic and electronic structure analysis.

Data availability

The authors declare that the main data supporting the findings of this work are available within the published article, its supplementary information, and source data files. All other relevant data are available from the corresponding author upon reasonable request. Source data are provided with this paper.

References

- Nastasi, M. & Mayer, J. W. Thermodynamics and kinetics of phase transformations induced by ion irradiation. *Mater. Sci. Rep.* **6**, 1–51 (1991).
- Zaiser, M. & Banhart, F. Radiation-induced transformation of graphite to diamond. *Phys. Rev. Lett.* **79**, 3680 (1997).
- Sickafus, K. et al. Radiation tolerance of complex oxides. *Science* **289**, 748–751 (2000).
- Sickafus, K. E. et al. Radiation-induced amorphization resistance and radiation tolerance in structurally related oxides. *Nat. Mater.* **6**, 217–223 (2007).
- Azarov, A. et al. Universal radiation tolerant semiconductor. *Nat. Commun.* **14**, 4855 (2023).
- Boulle, A. & Debelle, A. Statistical Nature of Atomic Disorder in Irradiated Crystals. *Phys. Rev. Lett.* **116**, 245501 (2016).
- Mason, D. R. et al. Observation of Transient and Asymptotic Driven Structural States of Tungsten Exposed to Radiation. *Phys. Rev. Lett.* **125**, 225503 (2020).
- Jiang, L. et al. Irradiation-Induced Extremes Create Hierarchical Face-/Body-Centered-Cubic Phases in Nanostructured High Entropy Alloys. *Adv. Mater.* **32**, 2002652 (2020).
- Uberuaga, B. P. et al. Opposite correlations between cation disordering and amorphization resistance in spinels versus pyrochlores. *Nat. Commun.* **6**, 8750 (2015).
- Barsoum, M. W. The $M_{n+1}AX_n$ phases: A new class of solids: Thermodynamically stable nanolaminates. *Prog. Solid State Chem.* **28**, 201–281 (2000).
- Radovic, M. & Barsoum, M. W. MAX phases: bridging the gap between metals and ceramics. *Am. Ceram. Soc. Bull.* **92**, 20–27 (2013).
- Sokol, M., Natsu, V., Kota, S. & Barsoum, M. W. On the Chemical Diversity of the MAX Phases. *Trends Chem.* **1**, 210–223 (2019).
- Younker, I. & Frattoni, M. Neutronic evaluation of coating and cladding materials for accident tolerant fuels. *Prog. Nucl. Energy* **88**, 10–18 (2016).
- Maier, B. R. et al. Cold spray deposition of Ti₂AlC coatings for improved nuclear fuel cladding. *J. Nucl. Mater.* **466**, 712–717 (2015).
- Tallman, D. J. et al. Effect of neutron irradiation on select MAX phases. *Acta Materialia* **85**, 132–143 (2015).
- Tallman, D. J. et al. Effects of neutron irradiation of Ti₃SiC₂ and Ti₃AlC₂ in the 121–1085 °C temperature range. *J. Nucl. Mater.* **484**, 120–134 (2017).
- Wang, C. et al. Disorder in $M_{n+1}AX_n$ phases at the atomic scale. *Nat. Commun.* **10**, 622 (2019).
- Wang, C. et al. Structural Transitions Induced by Ion Irradiation in V₂AlC and Cr₂AlC. *J. Am. Ceram. Soc.* **99**, 1769–1777 (2016).
- Wang, C. et al. Role of the X and n factors in ion-irradiation induced phase transformations of $M_{n+1}AX_n$ phases. *Acta Materialia* **144**, 432–446 (2018).
- Deng, T. et al. Ti₃AlC₂, a candidate structural material for innovative nuclear energy system: The microstructure phase transformation and defect evolution induced by energetic heavy-ion irradiation. *Acta Materialia* **189**, 188–203 (2020).
- Pang, L. et al. Phase transitions and He bubble evolution under sequential He ions implantation and Fe ions irradiation: New insight into the irradiation resistant of Ti₃AlC₂. *J. Eur. Ceram. Soc.* **42**, 7421–7429 (2022).
- Li, Y. et al. Defect formation energies in A₂B₂O₇ pyrochlores. *Scr. Materialia* **107**, 18–21 (2015).
- Zhao, S., Xue, J., Wang, Y. & Huang, Q. Ab initio study of irradiation tolerance for different $M_{n+1}AX_n$ phases: Ti₃SiC₂ and Ti₃AlC₂. *J. Appl. Phys.* **115**, 023503 (2014).
- Zhang, H. F. et al. Roles of silicon-layer in Ti₃SiC₂ materials response to helium irradiation: New insights from first-principles calculation. *Acta Materialia* **97**, 50–57 (2015).
- Xiao, J. et al. Investigations on Radiation Tolerance of $M_{n+1}AX_n$ Phases: Study of Ti₃SiC₂, Ti₃AlC₂, Cr₂AlC, Cr₂GeC, Ti₂AlC, and Ti₂AlN. *J. Am. Ceram. Soc.* **98**, 1323–1331 (2015).
- Shah, S. H. & Bristowe, P. D. Point defect formation in M₂AlC (M = Zr, Cr) MAX phases and their tendency to disorder and amorphize. *Sci. Rep.* **7**, 9667 (2017).
- Bugnet, M., Mauchamp, V., Oliviero, E., Jaouen, M. & Cabioc'h, T. Chemically sensitive amorphization process in the nanolaminated Cr₂AlC (A=Al or Ge) system from TEM in situ irradiation. *J. Nucl. Mater.* **441**, 133–137 (2013).

28. Wang, C., Tracy, C. L. & Ewing, R. C. Radiation effects in $M_{n+1}AX_n$ phases. *Appl. Phys. Rev.* **7**, 041311 (2020).
29. Huang, M., Li, Y., Ran, G., Yang, Z. & Wang, P. Cr-coated Zr-4 alloy prepared by electroplating and its in situ He⁺ irradiation behavior. *J. Nucl. Mater.* **538**, 152240 (2020).
30. Imtyazuddin, M., Mir, A. H., Tunes, M. A. & Vishnyakov, V. M. Radiation resistance and mechanical properties of magnetron-sputtered Cr₂AlC thin films. *J. Nucl. Mater.* **526**, <https://doi.org/10.1016/j.jnucmat.2019.151742> (2019).
31. Yang, T. et al. Formation of nano-twinned structure in Ti₃AlC₂ induced by ion-irradiation. *Acta Materialia* **128**, 1–11 (2017).
32. Su, R., Zhang, H., Liu, L., Shi, L. & Wen, H. Reversible phase transformation in Ti₂AlC films during He radiation and subsequent annealing. *J. Eur. Ceram. Soc.* **41**, 6309–6318 (2021).
33. Niu, C., LaRosa, C. R., Miao, J., Mills, M. J. & Ghazisaeidi, M. Magnetically-driven phase transformation strengthening in high entropy alloys. *Nat. Commun.* **9**, 1363 (2018).
34. Wu, Y. et al. Ductilizing Bulk Metallic Glass Composite by Tailoring Stacking Fault Energy. *Phys. Rev. Lett.* **109**, 245506 (2012).
35. Vedmedenko, O., Röscher, F. & Elsässer, C. First-principles density functional theory study of phase transformations in NbCr₂ and TaCr₂. *Acta Materialia* **56**, 4984–4992 (2008).
36. Chisholm, M. F., Kumar, S. & Hazzledine, P. Dislocations in complex materials. *Science* **307**, 701–703 (2005).
37. Yu, R., Zhan, Q., He, L., Zhou, Y. & Ye, H. Stacking faults and grain boundaries of Ti₃SiC₂. *Philos. Mag. Lett.* **83**, 325–331 (2003).
38. Mayr, S. G. & Averback, R. S. Effect of ion bombardment on stress in thin metal films. *Phys. Rev. B* **68**, 214105 (2003).
39. Azarov, A. et al. Disorder-Induced Ordering in Gallium Oxide Polymorphs. *Phys. Rev. Lett.* **128**, 015704 (2022).
40. Van De Walle, A., Asta, M. & Ceder, G. The alloy theoretic automated toolkit: A user guide. *Calphad* **26**, 539–553 (2002).
41. Zunger, A., Wei, S. H., Ferreira, L. G. & Bernard, J. E. Special quasirandom structures. *Phys. Rev. Lett.* **65**, 353–356 (1990).
42. Henkelman, G., Uberuaga, B. P. & Jónsson, H. A climbing image nudged elastic band method for finding saddle points and minimum energy paths. *J. Chem. Phys.* **113**, 9901–9904 (2000).
43. Ogata, S., Li, J. & Yip, S. Ideal pure shear strength of aluminum and copper. *Science* **298**, 807–811 (2002).
44. Otero-de-la-Roza, A., Johnson, E. R. & Luaña, V. Critic2: A program for real-space analysis of quantum chemical interactions in solids. *Comput. Phys. Commun.* **185**, 1007–1018 (2014).
45. Bader, R. *Atoms in molecules: a quantum theory* (Oxford Univ. Press, 1990).
46. Song, H. et al. Local lattice distortion in high-entropy alloys. *Phys. Rev. Mater.* **1**, 023404 (2017).
47. Granberg, F. et al. Mechanism of Radiation Damage Reduction in Equiatomic Multicomponent Single Phase Alloys. *Phys. Rev. Lett.* **116**, 135504 (2016).
48. Kioussis, N., Herbranson, M., Collins, E. & Eberhart, M. E. Topology of electronic charge density and energetics of planar faults in fcc metals. *Phys. Rev. Lett.* **88**, 125501 (2002).
49. Qi, Y. & Mishra, R. K. Ab initio study of the effect of solute atoms on the stacking fault energy in aluminum. *Phys. Rev. B* **75**, 224105 (2007).
50. Atkins, P. *Shriver and Atkins' inorganic chemistry* (Oxford University Press, USA, 2010).
51. Emsley, J. *The elements*, 3rd edn. (Clarendon Press, 1998).
52. Zhao, S. Lattice distortion in high-entropy carbide ceramics from first-principles calculations. *J. Am. Ceram. Soc.* **104**, 1874–1886 (2021).
53. Lapauw, T. et al. The double solid solution (Zr, Nb)₂(Al, Sn)C MAX phase: a steric stability approach. *Sci. Rep.* **8**, 12801 (2018).
54. Tunca, B. et al. Synthesis and Characterization of Double Solid Solution (Zr,Ti)₂(Al,Sn)C MAX Phase Ceramics. *Inorg. Chem.* **58**, 6669–6683 (2019).
55. Pauling, L. The nature of the chemical bond. IV. The energy of single bonds and the relative 550 electronegativity of atoms. *J. Am. Chem. Soc.* **54**, 3570–3582 (1932).
56. Sanderson, R. T. Electronegativity and bond energy. *J. Am. Chem. Soc.* **105**, 2259–2261 (1983).
57. Zhao, S. et al. Phase transformation and amorphization resistance in high-entropy MAX phase M₂SnC (M= Ti, V, Nb, Zr, Hf) under in-situ ion irradiation. *Acta Materialia* **238**, 118222 (2022).
58. Qarra, H. H., Knowles, K. M., Vickers, M. E., Akhmedaliev, S. & Lambrinou, K. Heavy ion irradiation damage in Zr₂AlC MAX phase. *J. Nucl. Mater.* **523**, 1–9 (2019).
59. Tian, W. et al. Synthesis and thermal and electrical properties of bulk Cr₂AlC. *Scr. Materialia* **54**, 841–846 (2006).
60. Hu, C. et al. In Situ Reaction Synthesis and Mechanical Properties of V₂AlC. *J. Am. Ceram. Soc.* **91**, 4029–4035 (2008).
61. Zhang, W., Travitzky, N., Hu, C., Zhou, Y. & Greil, P. Reactive Hot Pressing and Properties of Nb₂AlC. *J. Am. Ceram. Soc.* **92**, 2396–2399 (2009).
62. Stoller, R. E. et al. On the use of SRIM for computing radiation damage exposure. *Nucl. Instrum. Methods Phys. Res. Sect. B* **310**, 75–80 (2013).
63. Mitchell, D. R. G. *HRTEM filter V1.3*, www.felmi-zfe.at/dm-script/dm-script-database/ (2007).
64. Kilaas, R. Optimal and near-optimal filters in high-resolution electron microscopy. *J. Microsc.* **190**, 45–51 (1998).
65. Kresse, G. & Furthmüller, J. Efficient iterative schemes for ab initio total-energy calculations using a plane-wave basis set. *Phys. Rev. B* **54**, 11169 (1996).
66. Kresse, G. & From, D. J. ultrasoft pseudopotentials to the projector augmented-wave method. *Phys. Rev. B* **59**, 1758 (1999).
67. Perdew, J. P., Burke, K. & Ernzerhof, M. Generalized gradient approximation made simple. *Phys. Rev. Lett.* **77**, 3865 (1996).
68. Pack, J. D. & Monkhorst, H. J. “Special points for Brillouin-zone integrations”—a reply. *Phys. Rev. B* **16**, 1748–1749 (1977).
69. Shang, S. L. et al. Generalized stacking fault energy, ideal strength and twinnability of dilute Mg-based alloys: A first-principles study of shear deformation. *Acta Materialia* **67**, 168–180 (2014).
70. Feng, L. et al. Localized phase transformation at stacking faults and mechanism-based alloy design. *Acta Materialia* **240**, <https://doi.org/10.1016/j.actamat.2022.118287> (2022).

Acknowledgements

We would like to thank Steven J. Zinkle and William J. Weber at the University of Tennessee, Ji Chen, Limei Xu, and Zhiyuan Huang at Peking University, and Hongliang Zhang and Liqun Shi at Fudan University for their fruitful discussions. The authors also acknowledge Jinchu Huang et al. at Xiamen University for their assistance during the ion irradiation experiments. This work was supported by the National Natural Science Foundation of China (Grant No. 12422514 and 12275009, C.W., 12192280 and 11935004, Y.W.), National MCF Energy R&D Program 2022YFE03110000, C.W., and Zhejiang Key Laboratory of Data-Driven High-Safety Energy Materials and Applications, Q.H and C.W.

Author contributions

C.W. and S.Z. conceived the study. S.Z., Y.L., Z.Z. and C.W. performed the experiments, analyzed the data, interpreted the results, and wrote the paper. H.X. performed part of the first principle calculation. Y.W., C.L.T., R.C.E. and F.G. contributed to the discussion and manuscript modification. Q.H. provided the bulk samples and L.C. helped with the irradiation experiment. C.W. supervised the work. All authors contributed to revising and approving the manuscript.

Competing interests

The authors declare no competing interests.

Additional information

Supplementary information The online version contains supplementary material available at <https://doi.org/10.1038/s41467-025-56921-8>.

Correspondence and requests for materials should be addressed to Chenxu Wang.

Peer review information *Nature Communications* thanks Philipp Franke, who co-reviewed with Maria Yankova, and the other, anonymous, reviewer(s) for their contribution to the peer review of this work. A peer review file is available.

Reprints and permissions information is available at <http://www.nature.com/reprints>

Publisher's note Springer Nature remains neutral with regard to jurisdictional claims in published maps and institutional affiliations.

Open Access This article is licensed under a Creative Commons Attribution-NonCommercial-NoDerivatives 4.0 International License, which permits any non-commercial use, sharing, distribution and reproduction in any medium or format, as long as you give appropriate credit to the original author(s) and the source, provide a link to the Creative Commons licence, and indicate if you modified the licensed material. You do not have permission under this licence to share adapted material derived from this article or parts of it. The images or other third party material in this article are included in the article's Creative Commons licence, unless indicated otherwise in a credit line to the material. If material is not included in the article's Creative Commons licence and your intended use is not permitted by statutory regulation or exceeds the permitted use, you will need to obtain permission directly from the copyright holder. To view a copy of this licence, visit <http://creativecommons.org/licenses/by-nc-nd/4.0/>.

© The Author(s) 2025